Nanoscale

ROYAL SOCIETY OF CHEMISTRY

PAPER

View Article Online
View Journal | View Issue

Cite this: *Nanoscale*, 2023, **15**, 8814

Manipulating morphology and composition in colloidal heterometallic nanopods and nanodendrites†

Siyi Ming and Andrew E. H. Wheatley *

Branched Pt nanoparticles represent an exciting class of nanomaterials with high surface areas suitable for applications in electrocatalysis. Introducing a second metal can enhance performance and reduce cost. External factors such as capping agents and temperature have been used to offer insights into nanopod formation and to encourage their kinetic evolution. More recently, nanodendrites have been reported, though synthesis has generally been empirical; making controlled variation of morphology while maintaining bimetallic composition an elusive target. We report the combination of Pt with Fe under a range of conditions, yielding individually bimetallic nanoparticles whose construction sheds new light on nanopod and/or nanodendrite formation. Fine control of metal precursor reduction through modulating capping agents, reagents, and temperature initially directs nanopod synthesis. Morphology control is retained while composition is then varied from Pt-rich to Pt-poor. Additionally, conditions are identified that promote the collision-based branching of nanopod arms. This allows synthesis to be redirected for the selective growth of compositionally controlled nanodendrites in predictable fashion.

Received 31st January 2023,
Accepted 15th April 2023

DOI: 10.1039/d3nr00461a

rsc.li/nanoscale

Introduction

Colloidal metal nanopartciles (NPs) have vast appeal as candidates in applications such as catalysis,[1] plasmonics,[2] imaging,[3] electronics,[4] sensing,[5] photonics,[6] medicine,[7] and as building blocks for nanoscale devices.[8] Controlling their shape is critical to tailoring their physicochemical properties and influencing performance, since the shape of a nanoparticle determines which crystal facets are exposed at its surface.[9–11] Additionally, surface composition plays an essential role in defining properties,[12] as element intermixing controls the details of active sites, electron donor/acceptor effects, interfacial properties, and the occurrence of surface defects.[13,14] Overall, control of shape and composition are vital to optimizing performance.[15]

Among the shapes reported for colloidal metal nanoparticles, branched morphologies,[16] such as nanopods[17] and nanodendrites,[18] have attracted interest. This is because while the catalytic activity of pseudospherical NPs has been linked to their high surface-area-to-volume ratios, this ratio is enhanced by branching.[9] This exposes more surface active sites[19] and allows the use of lower catalyst loadings.[20] However, branched nanostructures have high surface energies and thermodynamically convert to pseudospheres or near-pseudospherical polyhedra by the migration of adatoms to exposed low energy facets.[21] Additionally, many NP catalysts are based on noble metals, whose face-centered cubic (fcc) structures disfavour anisotropic growth.[22]

The syntheses of branched NPs for transition metals, including Pt,[23] Ni,[24] Co,[25] Pd,[21] Ag,[26] Au,[27] and advances in making individually bimetallic alloys,[17,28–32] have been reported. In particular, for nanopods, external factors encourage kinetic NP growth, whereby high-energy facets evolve faster than low-energy facets, yielding branched nanoparticles.[16] These external factors can include capping agents and mixtures thereof that selectively cap specific facets,[33–36] or temperature and precursor concentration that encourage growth in the kinetic regime.[20,37] Two theories have been developed to explain branching; atomic deposition[38] and oriented attachment.[39] In the first, atoms continuously add to high energy NP facets, with branching seen when the deposition rate exceeds that of the subsequent migration of these adatoms to lower energy facets.[16] In the second, nanocrystallites coalesce before reorienting to co-align their crystallographic orientations.[40] (Methods like selective etching[33,41] and template-directed growth[42] have been investigated, but bring cost and complexity.) However, progress with morphology control in nanopods has not been accompanied by an ability to concurrently control particle composition in multimetallic

Yusuf Hamied Department of Chemistry, University of Cambridge, Lensfield Road, Cambridge, CB2 1EW, UK. E-mail: aehw2@cam.ac.uk

† Electronic supplementary information (ESI) available. See DOI: https://doi.org/10.1039/d3nr00461a

systems. In turn, this is important because compositional changes reflect competition between (1) rates of metal atom production, (2) particle seeding, collision and reorientation, and (3) atomic deposition and migration. These effects further feed into the shape and size of the resulting NPs.[17,43] It is, therefore, of primary importance – yet still extremely challenging – to controllably manipulate both nanopod shape and composition.

Moving from nanopods to nanodendrites, synthesis has hitherto been essentially empirical, with growth mechanisms eluding full explanation.[44–47] Simulations of dendrite formation by diffusion-limited aggregation suggest randomly diffusing preformed NPs attach sequentially to a seed particle to evolve a dendrite structure.[48–50] While this stepwise mechanism is artificial, it is accepted that a similar collision motif can explain randomized nanoobjects, particularly at high NP concentrations.[51,52] However, a more rigorous understanding of the growth mechanism(s) promises a unified approach and the targeted design of nanopods and nanodendrites.

In this paper, Pt is systematically combined with Fe in one-pot processes using routine reagents. Reactions done under a range of conditions yield individually bimetallic nanoparticles whose construction sheds new light on the growth mechanisms operating during nanopod and nanodendrite formation. Initially, the importance of avoiding excess nucleation in the formation of nanopods is highlighted. Thereafter, the fine control of capping agent and reductant addition, metal reagent addition, and temperature is used to manipulate nucleation and growth steps. This enables the controlled variation of morphology and of composition. Finally, the maintenance of a controlled nanopod level in reaction systems underpins the establishment of a collision-based mechanism whereby nanopod arms undergo branching. Control of nanopod levels is then used to predictably and selectively achieve nanodendrites.

Experimental section

General experimental

1,2-Hexadecanediol (1,2-HDD, 90%), oleic acid (OA, 90%), oleylamine (OAm, 70%), $Ni(acac)_2$ (95%) were purchased from Sigma-Aldrich. $Pt(acac)_2$ (98%) and $Fe(acac)_3$ (97%) were from Acros Organics. All materials were used as supplied with no further purification. Hexane was freshly distilled off Na/K amalgam.

Synthesis

Pt/Fe NPs: $Pt(acac)_2$ (98.3 mg, 0.25 mmol) and $Fe(acac)_3$ (88.4 mg, 0.25 mmol) were placed under N_2 by purging their containment vessel 3 times. They were treated with OA (x mL) and OAm (y mL) (for exact quantities see figure legends) after which the atmosphere was purged a further 3 times. The mixture was magnetically stirred at 1000 rpm and heated under N_2 at 105 °C for 3 min. 1,2-HDD (193.83 mg, 0.75 mmol) was promptly added under a positive flow of N_2, after which a further 3 purges of the atmosphere were carried out and heating was continued at 105 °C for another 2 min. Finally, the mixture was heated at 250 °C (alternatively 225 or 300 °C, as specified in figure legends) for 30 min (or 15 min, if specified in figure legends). The heating source was removed but stirring was maintained. Upon cooling to room temperature, freshly distilled hexane (2 mL) was added into the vessel to prevent precipitation. The obtained product was washed by centrifugation in ethanol (45 mL, 5500 rpm, 10 min) two times before being re-dispersed in distilled hexane (10 mL).

Pt/Fe NPs using 2 : 1 Pt : Fe: The protocol described in the 1 : 1 synthesis was modified to use $Fe(acac)_3$ (44.2 mg, 0.125 mmol).

Pt/Fe NPs using 5 : 1 Pt : Fe: The protocol described in the 1 : 1 synthesis was modified to use $Fe(acac)_3$ (17.7 mg, 0.05 mmol).

Pt/Fe NPs with mixing at 200 °C: The protocol described in the 1 : 1 synthesis was modified to use $Fe(acac)_3$ (44.2 mg, 0.125 mmol). After 1,2-HDD addition and 2 min heating at 105 °C, the reaction mixture was heated at 200 °C for z mins (for time see figure legends), before the temperature was elevated to 250 °C for 30 min.

Pt/Ni NPs with mixing at 200 °C: The protocol in the 1 : 1 Pt : Fe synthesis was modified by treating $Pt(acac)_2$ (98.3 mg, 0.25 mmol) and $Ni(acac)_2$ (64.2 mg, 0.25 mmol) with OA (0.4 mL) and OAm (1.2 mL). After 1,2-HDD addition and 2 min heating at 105 °C, the reaction mixture was heated at 200 °C for z mins (for time see figure legend), before the temperature was elevated to 250 °C for 30 min.

Characterization

For transmission electron microscopy (TEM) analysis, washed products re-dispersed in hexane were sonicated for 5 min before drop-casting onto a lacey carbon 300 mesh copper grid (Agar Scientific). The grid was plasma cleaned for 40 s. using a Fischione Model 1070 Nanoclean before analysis was performed using a Thermo Scientific (FEI) Talos F200X G2 TEM operating at 200 kV. TEM images were acquired using a Ceta $4k \times 4k$ CMOS (complimentary metal oxide semiconductor) camera. Energy dispersive X-ray (EDX) analysis was performed in scanning TEM (STEM) mode. Images were acquired using a high-angle annular dark field (HAADF) detector and EDX spectra/maps were collected using a Super-X detector system, which consists of 4 windowless silicon drift detectors.

Powder X-ray diffraction patterns were measured on a PANalytical Empyrean diffractometer fitted with an X'celerator detector and a Cu-Kα_1 (λ = 1.5406 Å) source, with a step size of 0.002° and scanning speed of 0.022° s^{-1} at 40 kV and 40 mA.

Inductively-coupled plasma-optical emission spectroscopy (ICP-OES) samples were prepared by suspension in a mixture of HCl (3.75 mL) and HNO_3 (1.25 mL), heating at 80 °C for 30 min, then diluting with water (5 mL), and allowing to settle overnight. A 0.5 mL aliquot of each was then diluted to 10 mL with water. Analysis for Fe and Pt was performed on a Thermo Fisher Scientific iCAP 7400 ICP-OES spectrometer against a standard curve (0.01–10 ppm). Standards were prepared by

diluting a commercial ICP-OES standard (Sigma-Aldrich) with 2% HNO_3. (The standards used for the curve were 0.01, 0.05, 0.1, 0.5, 1, 2.5, 5, 7.5 and 10 ppm.)

Results and discussion

Strategy development

Varying the type and relative concentration of chemical species such as reducing agent(s) and metal salt(s), as well as changing conditions like temperature, have previously been effective in controlling the shapes of NPs through changes to the overall rate of metal ion reduction.[20] However, for heterobimetallic systems any change can alter both morphology and composition.[17,43,53] Hitherto, one practical effect of the way Pt-based bimetallics have been targeted was that product formation was significantly affected by the noble metal's positive reduction potential and products were therefore Pt-rich or equimolar.[17,43,54,55] We reasoned that more effective compositional variations could be achieved by using multiple variables to ensure a thermodynamic reaction pathway (Scheme 1(a)). Changes to composition in bimetallic NPs are generally accompanied by morphological changes.[17,30] By logical extension though, understanding the symbiotic relationship between multiple condition changes would offer to maintain morphology while varying composition and *vice versa*. This should make it possible to obtain low-Pt products and to manipulate either morphology or composition.

Solution-phase NP synthesis comprises nucleation and growth processes. Though shape and twinning of nuclei can influence final NP morphology,[56] the dominant effect is had by growth,[10] which is either thermodynamically or kinetically controlling, giving rise to different morphologies. Examples of this, shown in Fig. 1(a)–(d), result from the synthetic approach we adopt here. Specifically, a 1 : 1 metal salt mixture has been treated with the same total volume (to ensure equivalent metal reagent concentrations) of capping agents oleic acid (OA) and oleylamine (OAm) and a strong reductant. The last is 1,2-hexadecanediol (1,2-HDD). Based on our previous work[57,58] and literature on Pt/Fe[59,60] and Pt/Ni[61,62] systems, these conditions are expected to ensure the smooth generation of Pt^0 and Fe^0 (see ESI† for confirmation from PXRD of this in the current work). While doing this, we have tested the symbiotic relationship between parameters that offers a route to modulate the morphological and compositional outcome of the reaction (Scheme 1(b)). Fig. 1(a) shows prototypical (near-)pseudospheres of the type expected from a low flux of reduced metal monomers (relatively low reduction rate) triggering thermodynamic growth (purple region in Fig. 1(e)). Any changes to

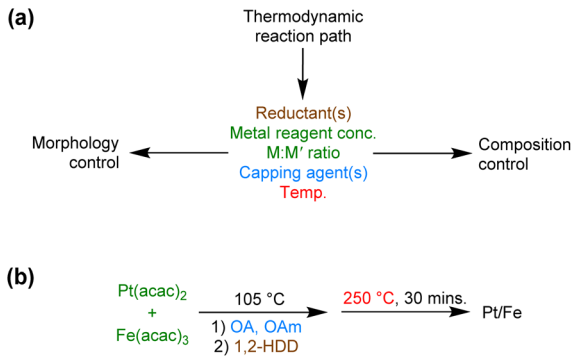

Scheme 1 (a) Symbiotically related variables that can be used to investigate dual composition and morphology control in anisotropic nanoparticles. (b) Summary of the protocol initially adopted in this work.

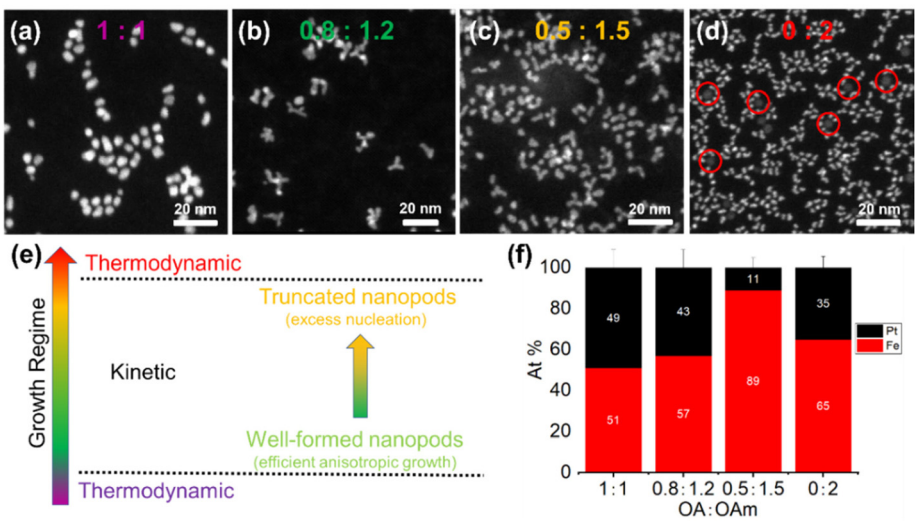

Fig. 1 (a)–(d) Representative HAADF images of Pt/Fe NPs synthesized at 250 °C using various OA : OAm ratios and a 1 : 1 Pt : Fe substrate ratio; (d) red circles highlight Fe-based pseudospheres generated alongside bimetallic seeds; (e) the different regimes available for product formation; (f) mean STEM EDX compositions from samples in (a)–(d) (error bars show standard deviation over 15 datasets; see Fig. S1;† for EDX analysis of (d) excluding pseudospheres see Fig. S7†).

the system that make conditions more reducing would be expected to shift the growth regime to kinetic control, giving anisotropic pod-like shapes. This is either because atomic deposition at high-energy facets now outstrips the migratory aptitude of adatoms to lower energy facets,[21] or because nanocrystallites undergo collision and oriented attachment.[39] In this regime, pod size and the extent of anisotropy would be influenced by the availability of feedstock in the growth phase. Hence, raising the reduction rate would give more nucleation (Fig. 1(e), green) but leave sufficient feedstock for the kinetic growth of larger particles. However, continuing to raise the rate (Fig. 1(e), yellow) would cause extensive nucleation and a truncated kinetic growth phase. These scenarios are illustrated in Fig. 1(b) and (c), respectively. Finally, the most strongly reducing conditions would cause reversion to the thermodynamic regime (Fig. 1(e), red) and near-pseudospheres (Fig. 1(d)), with particle growth at all facets or with sufficient thermal energy to migrate surface atoms to lower energy facets. These arguments guided our initial attempts to systematically contrive the growth of anisotropic Pt/Fe NPs.

The role of capping agents

Steric capping agents are fundamental controllers of NP development, and combining alkylamines with carboxylic acids and/or phosphines and thiols offers fine-control over products.[63] This work utilizes the fact that OA and OAm capping agents both combine to induce a range of product morphologies,[64] and that they can offer multifunctionality. OA generally acts as a facet-indiscriminate capping agent,[65] and increasing its contribution induces only a transition away from anisotropic growth and the agglomeration of pseudospheres.[43,57] In contrast, OAm is established as acting as a facet-selective capping agent[65] and reductant.[58,63,66] Harnessing this promises an additional level of fine-control over the reducing power available in our systems, and this is investigated in Fig. 1(a)–(d) (see ESI, Fig. S1†).‡ Data show the results of initial experiments where equimolar Pt:Fe mixtures were treated with 1,2-HDD at 250 °C, with increases in the proportion of OAm relative to OA (maintaining a 2 mL total volume of the two to ensure constant initial metal reagent concentrations in each experiment) gradually rendering the system more strongly reducing. Fig. 1(a) shows small pseudospherical seeds made with 1 : 1 OA : OAm, suggesting a modest reduction rate (Fig. 1(e), purple). Increasing the proportion of OAm gives nanopods, with arm formation giving larger particles on account of an initial nucleation event that leaves sufficient feedstock for subsequent kinetic anisotropic growth (Fig. 1(b), green; compare 4.7 ± 1.1 nm *vs.* 8.6 ± 1.6 nm in Fig. S2†). More strongly reducing conditions next induce more nucleation that consumes potential feedstock for growth and yields smaller nanopods (Fig. 1(c), yellow; 4.3 ± 0.8 nm in Fig. S2†). This situation is exacerbated if the rate (proportion of OAm) is further increased, with rapid reduction now causing extensive nucleation and inhibiting anisotropic growth (Fig. 1(d); 3.5 ± 0.6 nm in Fig. S2†). A closer inspection of this high-angle annular dark field (HAADF) figure reveals that alongside the small, brightly contrasting particles, large and less clearly contrasting pseudospheres have formed (examples circled red, see below). Scanning transmission electron microscopy (STEM) energy dispersive X-ray (EDX) maps of the 0.8 : 1.2 and 0 : 2 OA : OAm systems establish that the brighter particles are uniformly intermixed and bimetallic (see Fig. S3 and S4†). Meanwhile, high-resolution (HR) TEM imaging points to anisotropic growth by collision-based oriented attachment; monocrystalline seeds form under strongly reducing conditions whereas nanopods generated under less strongly reducing conditions show randomly oriented lattice fringes attributable to the 111 and 200 planes of fcc PtFe (Fig. S5†).[67,68] Data suggest the relatively short reaction time prevents the crystallographic alignment of aggregated seeds.

Moving to composition, Pt(II) can be more easily reduced than Fe(III), to create Pt-rich bimetallic NPs through a kinetically controlled reaction.[69] In this work, we aim to avoid this. From Fig. 1(f), Pt_1Fe_1 forms if both metal precursors and capping agents OA and OAm are each used in 1 : 1 ratios. If the proportion of OAm is then increased, product composition can be skewed towards Fe. In particular, for OA : OAm 0.5 : 1.5, the product reveals an Fe contribution of ~90 At%. However, when only 2 mL OAm is used (*i.e.* OA is excluded), this drops to ~65 At%. As noted above, this sample also reveals the appearance of pseudospherical NPs. These analyze as Fe-based by STEM EDX (Fig. S4†), suggesting the formation of Fe NPs that oxidize to magnetite.[64] While they are not common enough to significantly affect composition in this sample (Fig. S7†), their development alongside truncated nanopods helps explain the depleted Fe-content of the latter relative to the more highly anisotropic nanopods obtained in the 0.5 : 1.5 system. Taken together, these data point to reduction preferentially depleting Pt(II), with any subsequent promotion of reduction by increasing the proportion of OAm favouring the reduction of Fe(III). This increases the Fe contribution in individually bimetallic particles and ultimately yields monometallic Fe NPs. To probe this further, we explored the mechanism operating by varying OA : OAm whilst maintaining a constant level of the former. According to the view above, this should result in Fe content initially increasing as OAm levels are raised, before dropping again in the most reducing systems.

Based on the results above, the Fe-rich product obtained when OA : OAm = 0.5 : 1.5 (Fig. 1c and Fig. S1(g)–(i)†) was investigated to see how morphology and composition changed when varying OAm (1–3 mL) while using constant OA (0.5 mL). Data are presented in Fig. S1, S2 and S8, S9.† The system in Fig. S8(a)–(c)† incorporates less OAm (and a lower reduction ability) than that in Fig. S1(g)–(i).† That the nanopods formed are marginally bigger (4.8 ± 0.9 nm in Fig. S9(a) *vs.* 4.3 ± 0.8 nm in Fig. S2(c)†) is attributed to volume dictating whether

‡ High-angle annular dark field (HAADF) and high-resolution transmission electron microscopy (HRTEM) imaging, scanning TEM (STEM) energy dispersive X-ray spectroscopy (EDX) analysis and maps, and powder X-ray diffraction (PXRD) data are available as ESI.†

the system is relatively dilute or concentrated. That is, while adding more OAm provides additional reductant, dilution of the metal salts offsets this, preventing distinctly larger NPs from forming. However, using yet more OAm, Fig. S8(d)–(f)† emerge. These contain similarly shaped but larger nanopods (6.4 ± 1.3 nm in Fig. S9(b)†), which suggest the additional OAm now has proportionately less diluting effect (see below) and that the increased reducing ability of more OAm more than offsets the influence of increased volume. The mean compositions for each sample shown in Fig. S8† reinforce the view established by Fig. 1(f) and Fig. S1(i),† that using additional OAm initially raises and then lowers Fe contribution in the bimetallic product. Interestingly, Fig. S8(d)–(l) and S9(b)–(d)† present similar morphologies, sizes and compositions. Overall, results back-up our view that adding OAm makes the system more reducing and that the first effect of this is to promote Fe(III) reduction and Fe inclusion, with more Pt finally incorporated under only the most reducing conditions. With this in mind, experiments next turned to investigating temperature effects.

The role of temperature

The influence of temperature was monitored using three branched samples. Representative imaging is shown in Fig. 2 with corresponding particle size analysis in ESI Fig. S10.† An OA : OAm ratio of 0.8 : 1.2 at 250 °C gives the nanopods shown in Fig. 2(b). The same process at 225 °C retains polycrystalline nanopods (Fig. 2(a) and Fig. S11, S12) though particle size is decreased (5.7 ± 1.5 nm *vs.* 8.6 ± 1.6 nm, Fig. S10†), while 300 °C decreases arm number and nanopod size to 6.4 ± 1.2 nm (Fig. 2(c) and Fig. S10, S11†). This is attributed to the reduction rate being greatly increased at higher temperature. As mentioned before, in this regime nucleation outstrips particle growth.

NPs in Fig. 2(d)–(f) are produced using the same total volume of capping agent as those in Fig. 2(a)–(c), but with a higher proportion of OAm. Hence, nanopods in Fig. 2(e) are smaller than those in Fig. 2(b) (4.3 ± 0.8 nm *vs.* 8.6 ± 1.6 nm), on account of the higher reducing ability of the former system. Fig. 2(f) (see also Fig. S13†) reveals similar performance to that in Fig. 2(c) at the higher temperature of 300 °C. However, looking at lower temperature syntheses, Fig. 2(d) suggests a weaker reducing ability than in Fig. 2(a) even though more OAm is present. This surprising result is reflected too by visual assessment of the samples, where the 0.5 : 1.5/225 °C sample is less intensely black than the 0.8 : 1.2/225 °C sample, suggesting a lower yield of NPs. Consistent with this, HAADF-STEM shows only very small particle sizes in this sample (Fig. S13†). These data suggest an effect due to OA that is only evident when the system is not rendered strongly reducing on account of high levels of OAm and/or high temperature and which is therefore only evidenced Fig. 2(a). A possible explanation is furnished by a previous report on the use of mixed OA–OAm systems. In that work, $Fe(acac)_3$ underwent ligand substitution to incorporate the oleate conjugate base of OA (OA′). The resulting complex, $Fe(acac)_x(OA')_y$, was shown to induce extensive nucleation.[63] In our work, any such behavior would be most significant in Fig. 2(a), and indeed those product nanopods are very Fe-rich. The same prior art pointed to higher temperatures or the use of a greater proportion of OAm depleting OA through a condensation reaction with the amine to yield weak reductant *N*-(*cis*-9-octadecenyl)-oleamide.[63]

Fig. 2(g)–(i) and Fig. S13† report samples prepared using 0.5 mL OAm more than comparable samples in Fig. 2(d)–(f). The effect on reducing ability at 225 °C is clear, with significantly more reduction giving nanopods, though still slightly smaller than those in Fig. 2(a) (4.2 ± 0.8 nm *vs.* 5.7 ± 1.5 nm). A similar, strongly reducing situation is seen in Fig. 2(h), where nanopods possess either more or more distinct arms and are bigger than those in Fig. 2(e) (6.4 ± 1.3 nm *vs.* 4.3 ± 0.8 nm, also see Fig. 1(b) and (c)). This effect is even more pronounced at 300 °C (*cf.* Fig. 2(f) and (i), 5.4 ± 0.9 nm *vs.* 7.2 ± 1.3 nm), suggesting that the higher temperature exacerbates the strongly reducing (OAm-rich) conditions, giving nanopods with increasingly well-defined arms.

Moving to composition, Fig. 2(j) shows how samples produced using OA : OAm = 0.5 : 1.5 and 0.5 : 2 present similar trends. In these, Pt inclusion increases with temperature, but products contain a lower proportion of Pt at any given temperature for the (less strongly reducing) 0.5 : 1.5 systems. Samples made using OA : OAm = 0.8 : 1.2 present mean compositions similar to the 0.5 : 2 system at 225 and 300 °C. However, at 250 °C results are quite different, and suggest that a higher proportion of OA enables a higher Pt composition at rather less than 300 °C. Overall, these data establish that products with not only specific shapes and sizes, but also desired compositions from low-Pt to approaching equimolar, can be made by manipulating both OA and OAm levels (absolute and relative) as well as temperature. Lastly, the systems in Fig. 2 were used to verify product stability. Data reported in Fig. S15† show the results of comparable experiments notwithstanding the use of 15 rather than 30 min of heating at either 250 or 300 °C. The similar morphologies and compositions testify to the nanomaterials prepared here being completely formed in <15 min and undergoing no further alterations. This contrasts with previous work, in which extended heating caused morphological changes.[70]

The role of substrate ratio

The ease with which Fe substrates are reduced in this work irrespective of capping agent levels and reaction temperature has so far precluded Pt-rich products. This being so, we halved the amount of Fe reagent to encourage anisotropic NPs with Pt > 50 At%. Fig. 3 presents results obtained with a 2 : 1 Pt : Fe substrate ratio (see also Fig. S16 for size distributions and S17 for compositional data†). The differences between products obtained and those resulting from 1 : 1 Pt : Fe syntheses are stark. Apart from any compositional changes, raising the proportion of OAm under Fe-deficient conditions induces a transition from nanopods to a mixture of nanopods and 20.4 ± 3.2 nm nanodendrites, in which the latter are very dominant

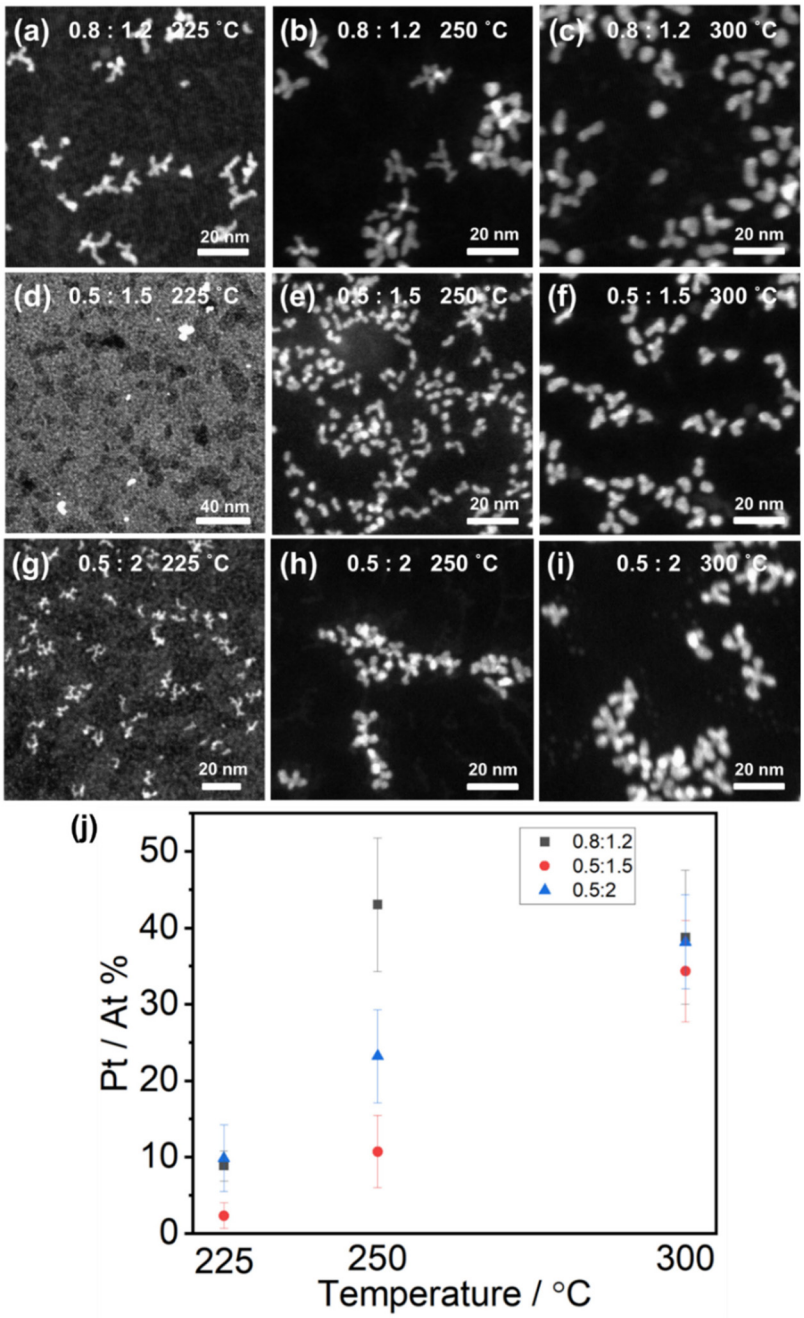

Fig. 2 Representative HAADF images of Pt/Fe NPs synthesized at different temperatures using OA : OAm 0.8 : 1.2 (a)–(c), 0.5 : 1.5 (d)–(f), 0.5 : 2 (g)–(i); (j) mean STEM EDX composition of particles shown in (a)–(i). Error bars show standard deviation over 15 datasets. For particle size distributions see Fig. S10.†

(Fig. 3(a), (b) and Fig. S16(a)†). Additional OAm completes this transition, giving the substantial (27.1 ± 4.7 nm) nanodendrites in Fig. 3(c) and Fig. S16(b).† Adding yet more OAm or raising temperature then causes reversion to nanopod formation. In the case of more OAm, nanopods co-exist with less large nanodendrites (20.3 ± 4.2 nm). Meanwhile, using 300 °C, only nanopods are seen (Fig. 3(d), (e) and Fig. S16(c)–(e)†).

More straightforward than the morphological variations in Fig. 3(a)–(e), the Pt contribution to products obtained using Fe-deficient conditions is increased, including to >50 At%. Overall, the two sets of compositional data in Fig. 3(f) still show similar trends; increasing reducing strength of the system initially raises Fe contribution to the product, before it finally falls back again (*viz.* Fig. 1 and Fig. S8†). However, the minimum in Pt contribution is shifted to higher OAm levels in the 2 : 1 Pt : Fe system. This is unsurprising given we now expect increased OAm to mainly promote Fe reduction. Moreover, we revisit an effect seen in Fig. S8,† where the

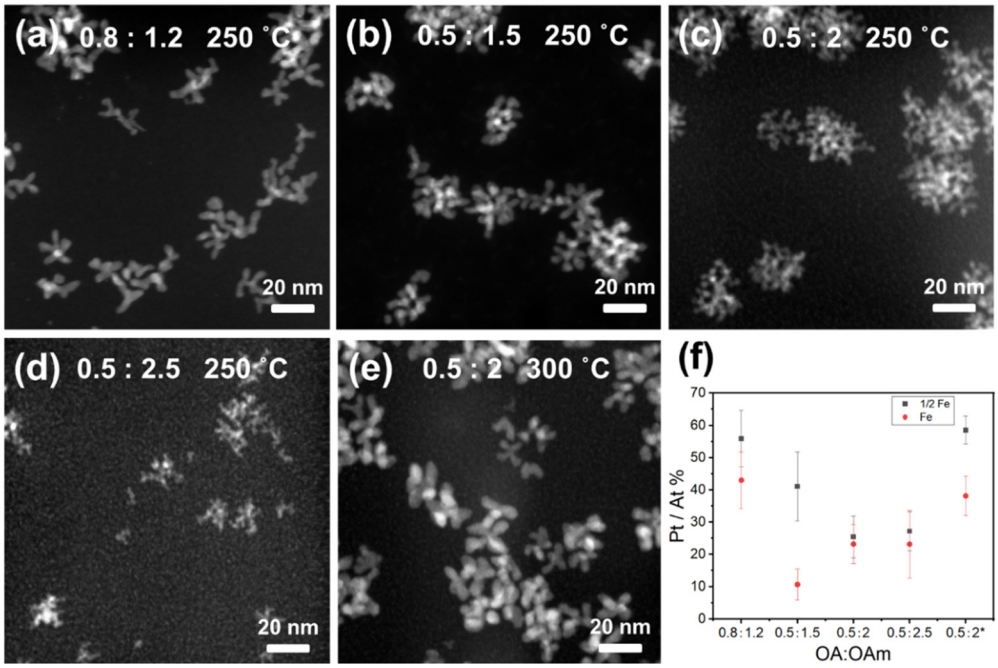

Fig. 3 Representative HAADF images of Pt/Fe NPs made at 250 °C or 300 °C using a Pt : Fe substrate ratio of 2 : 1 and OA : OAm 0.8 : 1.2 (a), 0.5 : 1.5 (b), 0.5 : 2 (c), 0.5 : 2.5 (d), 0.5 : 2 (e); (f) mean STEM EDX compositions from (a)–(e) (black) compared with those in Fig. 2 and S8(i)† (red). Error bars reflect standard deviation over 15 datasets. *300 °C reaction.

samples illustrated in Fig. 3(c) and (d) display equivalent compositions in spite of the use of additional OAm. Again, the offsetting of stronger reducing ability by increased volume is suggested.

Nanodendrites have previously been produced largely empirically.[44–47] However, these new data suggest a method for doing this predictably, potentially also controlling arm numbers. Current results suggest that making the system more strongly reducing (more OAm, higher temperature) raises the concentration of nanopods, and that this triggers nanodendrite formation (Fig. 3(a) and (b)). Further increasing nanopod concentration using more OAm continues this trend, with Fig. 3(c) showing more complex, larger nanodendrites. However, the continued addition of OAm then reaches a point where increased reducing ability is offset by the diluting influence of increased volume; this explains Fig. 3(d), where both nanopods and nanodendrites are seen. The data in Fig. 3(e) suggest the nanopod concentration is important in dictating whether nanodendrites form. This sample exhibits nanopods even though it should have a higher nanopod concentration due to the higher temperature. Overall, data suggest that moving from low to intermediate nanopod concentrations favours dendrite formation, but that continuing to raise this concentration then causes nanopods to be retained. This suggests the collision-based formation of nanodendrites, with low nanopod concentrations (weakly reducing systems) not exhibiting enough collisions. In very strongly reducing conditions (excess OAm), we speculate that nanopods express a surfactant double layer with OA closest to the particle surface and OAm forming an outer layer, and that this hinders collisions. The resulting avoidance of agglomeration leads nanopods synthesized in 0.5 : 2.0 OA : OAm at 300 °C to be highly stable – resisting separation by centrifugation, and remaining dispersed in hexane for weeks without precipitation. Similar behaviour has been seen for gold NPs in hexane stabilized by OA and OAm.[71]

Nanopod formation can be ascribed to seeds undergoing rapid atomic deposition or particle collisions. Polycrystallinity in Fig. S3† suggests the latter in our case, with short reaction times preventing the crystallographic realignment of individual nanocrystallites. HRTEM data obtained for the nanopodal 0.8 : 1.2 OA : OAm system in Fig. 3(a) support this view (Fig. S18†). Meanwhile, similar data for the 0.5 : 2.0 OA : OAm system, extend the idea to uniformly intermixed polycrystalline nanodendrites (Fig. 3(c) and Fig. S20†), before a reversion to polycrystalline nanopods is seen at higher temperature (Fig. 3(e) and Fig. S21†).

Conditions for nanodendrite formation

Based on the points outlined above, we hypothesize that a suitable nanopod concentration is key to triggering nanodendrite formation. "Suitable" means one high enough for diffusion-controlled aggregation but not requiring the use of excessive capping agents. In this concentration range, the arms of some nanopods become branched by virtue of coalescence events that occur following collisions between themselves and other nanopods (Scheme 2). We tested this idea by carefully controlling nanopod concentration and so manipulating both the emergence of nanodendrites and their complexity. To achieve this, a low-temperature step (200 °C, step 1) was inserted at the

Scheme 2 Proposed mechanism for making polycrystalline nanodendrites. Nanopods form initially (left). Subsequent collisions result in branching of the arms in some nanopods, giving nanodendrites (middle). Continued collisions between nanopods and the arms of nanodendrites exhausts the supply of nanopods (right).

start of the synthesis, during which seed particles should be created. Elevating the system to the usual reaction temperature would then allow reduction of the remaining feedstock (250 °C for 30 min, step 2). Three possible outcomes were envisaged depending on the duration of step 1. First, few seeds might form during a short step 1, with there being no or little influence on the consumption of monomer in step 2. This would allow sufficient nucleation in this step for nanopods to result. Second, a significant number of seeds could form if step 1 was of intermediate duration. Feedstock depletion would then restrict (or even prevent) nucleation in step 2, limiting nanopod generation and triggering nanodendrite formation. Third, extensive nucleation in an extended step 1 would give a dearth of feedstock for nucleation in step 2, but the nanopod concentration already achieved would be higher than that at which nanodendrites form.

Pt/Fe nanopods and nanodendrites made using 2 : 1 Pt : Fe reagents and a 0.8 : 1.2 OA : OAm volume ratio (total volume 2 mL) were tested and data are shown in Fig. 4(a)–(c) and Fig. S22, S23.† Microscopy on product obtained if step 1 was omitted (t = 0 min) reveals nanopod formation (Fig. 4(a)). A transition to nanodendrites is seen if step 1 lasted 10 min (Fig. 4(b)) before, in line with expectation, creating a higher concentration of seeds (20 min step 1) led to nanopods again dominating (Fig. 4(c)). While different morphologies are incurred, it is important to look for compositional variations.

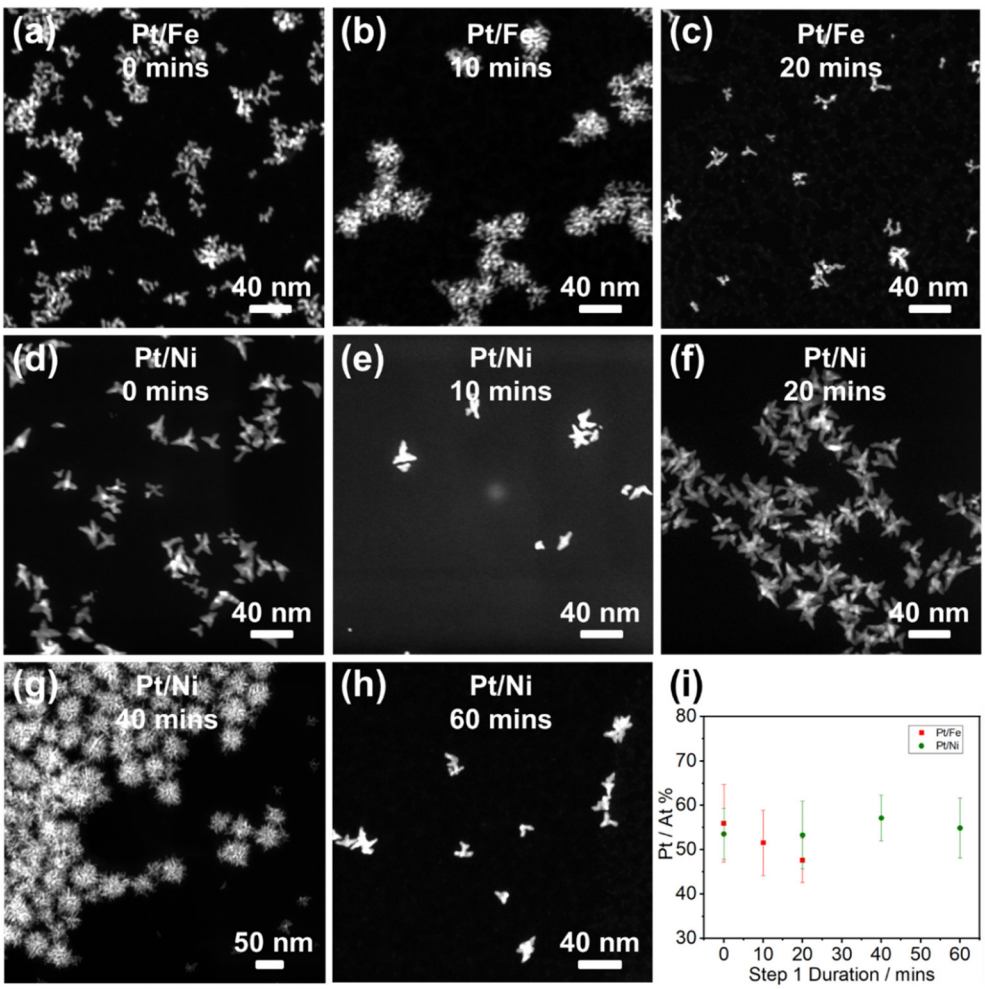

Fig. 4 (a)–(c) Representative HAADF images of Pt/Fe NPs made using 2 : 1 Pt : Fe and 0.8 : 1.2 mL OA : OAm at 250 °C for 30 min after mixing at 200 °C for 0–20 min; (d)–(h) Representative HAADF images of Pt/Ni NPs synthesized using 1 : 1 Pt : Ni and 0.4 : 1.2 mL OA : OAm at 250 °C for 30 min after mixing at 200 °C for 0–40 min; (i) Pt (At%) as a function of 200 °C mixing time (step 1) for products in (a)–(h).

In this case, though composition in fact remains within error (Fig. 4(i)), it is tempting to consider that extending step 1 yields a drop in Pt contribution. If genuine, this could be attributed to the ease of Fe(III) reduction.

Given the ambiguity over whether Pt/Fe composition alters in tests with a 200 °C mixing step, we undertook a similar study using equimolar $Pt(acac)_2$ and $Ni(acac)_2$ and a 0.4 : 1.2 OA : OAm volume ratio (total volume 1.6 mL). Step 1 (mixing at 200 °C for 0–60 min) preceded an unchanged step 2 (250 °C for 30 min), with the longer Step 1 offering greater scope to probe for compositional variations as a function of mixing time. Fig. 4(d) and (e) show that nanopods formed with either no or a short 200 °C step (t = 0, 10 min, also Fig. S24†). Using a 20 min mixing step increases the morphological complexity of the product (Fig. 4(f)), which we attribute to simple nanodendrites (27.8 ± 4.6 nm, Fig. S24 and S25†). In line with expectation, moving to a 40 min mixing step yields the much more substantial (45.0 ± 7.7 nm) dendrites of fcc PtNi seen in Fig. 4(g) and Fig. S24–S26.†[67] As now expected, a 60 min step 1 yields nanopods once more (Fig. 4(h) and Fig. S24†). These data plainly suggest a method for the controlled and selective formation of nanopods and nanodendrites in different bimetallic systems. The greater range of mixing times also allows a more confident analysis of composition in Ni/Pt nanopods/-dendrites; all samples demonstrate essentially identical compositions (Fig. 4(i)), verifying the ability to modulate morphology but maintain composition.

Pt-rich anisotropic growth

Lastly, this work has so far yielded either Fe-rich (Fig. 1), equimolar (Fig. 1 and 3) or modestly Pt-rich materials (Fig. 3). However, substantially Pt-rich nanopods and nanodendrites have yet to be achieved. To overcome this, we modified the protocols that gave the products illustrated in Fig. 3(a) and (e) to use 1 : 0.2 Pt : Fe by moles. Fig. S27 and S28† show the resulting nanodendrites (using 0.8 : 1.2 OA : OAm at 250 °C) and

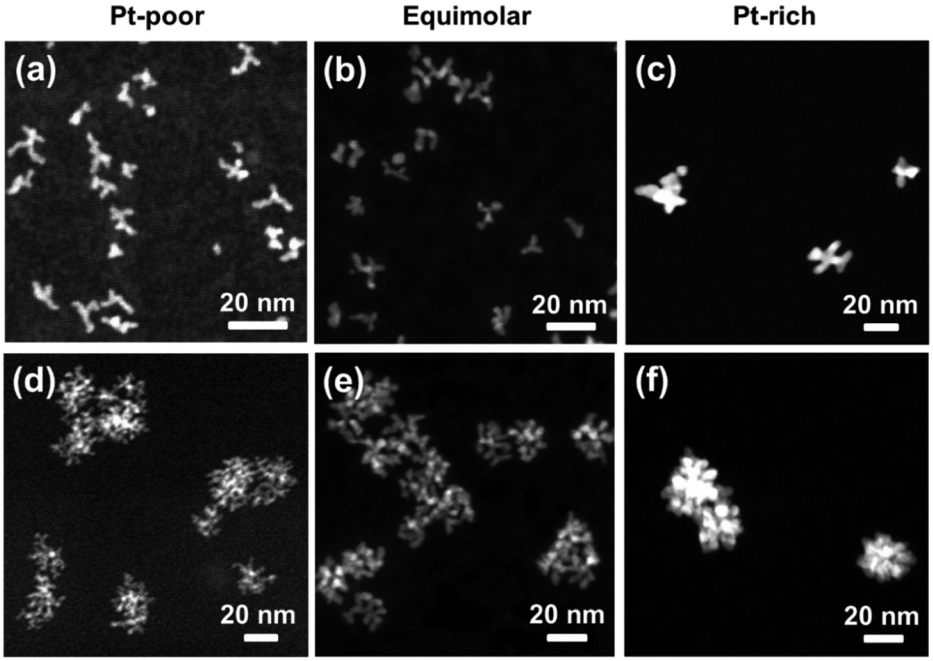

(g)

Image	Sample	Protocol[a]	EDX / At%	ICP / At%
(a)	Pt-poor, nanopod	1:1, 0.8:1.2, 225	8.8±2.0	14.2
(b)	Equimolar, nanopod	1:1, 0.8:1.2, 250	43.0±8.8	45.5
(c)	Pt-rich, nanopod	1:0.2, 0.5:2, 300	76.3±4.7	82.3
(d)	Pt-poor, nanodendrite	2:1, 0.5:2, 250	25.5±6.5	29.4
(e)	Equimolar, nanodendrite	2:1, 0.5:1.5, 250	41.1±10.7	51.0
(f)	Pt-rich, nanodendrite	1:0.2, 0.8:1.2, 250	76.3±6.0	81.5

[a]Pt:Fe reagents (ratio by moles), OA:OAm (ratio by mL), Temp. (°C)

Fig. 5 HAADF summary of outcomes for making Pt-deficient, equimolar and Pt-rich nanopods ((a)–(c)) and nanodendrites ((d)–(f)) using the conditions described in (g). STEM EDX data (means and standard deviations of 8 randomly selected regions) independently corroborated by ICP-OES analysis.

nanopods (0.5 : 2 OA : OAm, 300 °C), whose relative morphologies conform to our expectations. STEM EDX shows that both products are uniformly intermixed bimetallics containing a mean of 76 At% Pt. Of further interest, the product illustrated in Fig. 3(a) (prepared using 1 : 0.5 Pt : Fe in 0.8 : 1.2 OA : OAm at 250 °C) does not form nanodendrites. Instead, these form only if the system is made more strongly reducing (by adding OAm). In contrast, using 1 : 0.2 Pt : Fe allows nanodendrite formation, suggesting an additional level of control when seeking particular morphologies with different compositions. Data are summarized in Fig. 5, where independent confirmation of the compositions of products illustrated comes from ICP-OES data.

Conclusions

While branched NPs represent an exciting avenue of research into nanomaterials with high surface areas, the empirical nature with which they have often been made has hindered attempts at their systematic production. In addition, the desire to introduce a second metal has added complexity; namely the tendency for a change in composition to promote morphological change, and *vice versa*. The difficulty of systematically changing just one variable has interfered significantly with applications development.

Here, the systematic combination of Pt with Fe under a range of conditions yields bimetallic NPs that undergo specific condition-dependent aggregation by a collision-based mechanism to yield either nanopods or nanodendrites. The result is an ability to transition from one regime to the other selectively and predictably for, as far as we are aware, the first time. The transition is based on reaction stoichiometry, meaning that morphology can be altered independently of composition. Meanwhile, capping agent and temperature have controlled composition independently of morphology. Taken together, these developments allow the selection of both morphology (nanopod, nanodendrite) *and* composition (Pt-poor to Pt-rich).

Our group is now extending these ideas to other bimetallic combinations, seeking to generate a wider understanding of Pt/M nanopods/-dendrites where M is a base, 3d metal. Following the preparation of Pt/M contenders with systematic composition and morphology control, they will be heterogenized for catalysis of the oxygen reduction reaction.

Data availability

 Open Data that support this study are available at **https://doi.org/10.17863/CAM.91857**.

Conflicts of interest

There are no conflicts of interest to declare.

Acknowledgements

S. Ming thanks CSC Cambridge for a scholarship. The EPSRC is also acknowledged for support of electron microscopy at Cambridge (Underpinning Multi-User Equipment; EP/P030467/1).

References

1 X. Tian, X. Zhao, Y. Q. Su, L. Wang, H. Wang, D. Dang, B. Chi, H. Liu, E. J. M. Hensen, X. W. Lou and B. Y. Xia, *Science*, 2019, **366**, 850–856.
2 P. Yang, J. Zheng, Y. Xu, Q. Zhang and L. Jiang, *Adv. Mater.*, 2016, **28**, 10508–10517.
3 S. D. Anderson, V. V. Gwenin and C. D. Gwenin, *Nanoscale Res. Lett.*, 2019, **14**, 188.
4 J. Zhu and M. C. Hersam, *Adv. Mater.*, 2017, **29**, 1603895.
5 J. Hou, M. Li and Y. Song, *Nano Today*, 2018, **22**, 132–144.
6 I. Venditti, *Materials*, 2017, **10**, 97.
7 M. Rai, A. P. Ingle, S. Birla, A. Yadav and C. A. dos Santos, *Crit. Rev. Microbiol.*, 2016, **42**, 1–24.
8 S. Kuyuldar, D. T. Genna and C. Burda, *J. Mater. Chem. A*, 2019, **38**, 21545–21576.
9 Y. Xia, Y. Xiong, B. Lim and S. E. Skrabalak, *Angew. Chem., Int. Ed.*, 2009, **48**, 60–103.
10 K. An and G. A. Somorjai, *ChemCatChem*, 2012, **4**, 1512–1524.
11 A. R. Tao, S. Habas and P. Yang, *Small*, 2008, **4**, 310–325.
12 C. Xie, Z. Niu, D. Kim, M. Li and P. Yang, *Chem. Rev.*, 2020, **120**, 1184–1249.
13 J. Solla-Gullón, F. J. Vidal-Iglesias and J. M. Feliu, *Annu. Rep. Prog. Chem., Sect. C: Phys. Chem.*, 2011, **107**, 263–297.
14 Z. Peng and H. Yang, *Nano Today*, 2009, **4**, 143–164.
15 T. S. Rodrigues, A. G. M. da Silva and P. H. C. Camargo, *J. Mater. Chem. A*, 2019, **7**, 5857–5874.
16 B. Lim and Y. Xia, *Angew. Chem., Int. Ed.*, 2011, **50**, 76–85.
17 W. Lei, M. Li, L. He, X. Meng, Z. Mu, Y. Yu, F. M. Ross and W. Yang, *Nano Res.*, 2020, **13**, 638–645.
18 S. Lu, K. Eid, D. Ge, J. Guo, L. Wang, H. Wang and H. Gu, *Nanoscale*, 2017, **9**, 1033–1039.
19 Z. Ma, Z. P. Cano, A. Yu, Z. Chen, G. Jiang, X. Fu, L. Yang, T. Wu, Z. Bai and J. Lu, *Angew Chem., Int. Ed.*, 2020, **59**, 18334–18348.
20 S. Cheong, J. D. Watt and R. D. Tilley, *Nanoscale*, 2010, **2**, 2045–2053.
21 J. Watt, N. Young, S. Haigh, A. Kirkland and R. D. Tilley, *Adv. Mater.*, 2009, **21**, 2288–2293.
22 H. L. Liu, F. Nosheen and X. Wang, *Chem. Soc. Rev.*, 2015, **44**, 3056–3078.
23 A. Abdelhafiz, B. Zhao, Z. Xiao, J. Zeng, X. Deng, L. Lang, Y. Ding, H. Song and M. Liu, *ACS Appl. Mater. Interfaces*, 2020, **12**, 49510–49518.
24 X. Liang, N. Liu, H. Qiu, C. Zhang, D. Mei and B. Chen, *Phys. Chem. Chem. Phys.*, 2017, **19**, 26718–26727.

25 E. J. Popczun, C. W. Roske, C. G. Read, J. C. Crompton, J. M. McEnaney, J. F. Callejas, N. S. Lewis and R. E. Schaak, *J. Mater. Chem. A*, 2015, **3**, 5420–5425.
26 B. Khodashenas and H. R. Ghorbani, *Arabian J. Chem.*, 2019, **12**, 1823–1838.
27 M. Grzelczak, J. Pérez-Juste, P. Mulvaney and L. M. Liz-Marzán, *Colloidal Synthesis of Plasmonic Nanometals*, ed. L. M. Liz-Marzán, Jenny Stanford, New York, 2020, ch. 6.
28 A. R. Poerwoprajitno, L. Gloag, J. Watt, S. Cychy, S. Cheong, P. V. Kumar, T. M. Benedetti, C. Deng, K.-H. Wu, C. E. Marjo, D. L. Huber, M. Muhler, J. J. Gooding, W. Schuhmann, D. W. Wang and R. D. Tilley, *Angew. Chem., Int. Ed.*, 2020, **59**, 15487–15491.
29 T. Ma and F. Liang, *J. Mater. Chem. C*, 2020, **124**, 7812–7822.
30 J. Mao, Y. Chen, J. Pei, D. Wang and Y. Li, *Chem. Commun.*, 2016, **52**, 5985–5988.
31 H. Ding, P. Wang, C. Su, H. Liu, X. Tai, N. Zhang, H. Lv, Y. Lin, W. Chu, X. Wu, C. Wu and Y. Xie, *Adv. Mater.*, 2022, **34**, 2109188.
32 S. Chen, M. Li, M. Gao, J. Jin, M. A. van Spronsen, M. B. Salmeron and P. Yang, *Nano Lett.*, 2020, **20**, 1974–1979.
33 T. H. Yang, Y. Shi, A. Janssen and Y. Xia, *Angew. Chem., Int. Ed.*, 2020, **59**, 15378–15401.
34 A. Alinezhad, T. M. Benedetti, L. Gloag, S. Cheong, J. Watt, H. S. Chen, J. J. Gooding and R. D. Tilley, *ACS Appl. Nano Mater.*, 2020, **3**, 5995–6000.
35 G. M. Leteba, G. M. Leteba, D. R. G. Mitchell, P. B. J. Levecque, L. Macheli, E. van Steen and C. I. Lang, *ACS Appl. Nano Mater.*, 2020, **3**, 5718–5731.
36 G. M. Leteba, D. R. G. Mitchell, P. B. J. Levecque, E. van Steen and C. I. Lang, *RSC Adv.*, 2020, **10**, 29268–29277.
37 G. M. Leteba, D. R. G. Mitchell, P. B. J. Levecque, E. van Steen and C. I. Lang, *Nanomaterials*, 2021, **11**, 1825.
38 K. D. Gilroy, X. Yang, S. Xie, M. Zhao, D. Qin and Y. Xia, *Adv. Mater.*, 2018, **30**, 1706312.
39 R. Chen, Q. N. Nguyen and Y. Xia, *ChemNanoMat*, 2022, **8**, e202100474.
40 X. Xue, R. L. Penn, E. R. Leite, F. Huang and Z. Lin, *CrystEngComm*, 2014, **16**, 1419–1429.
41 G. M. Leteba, Y. C. Wang, T. J. A. Slater, R. Cai, C. Byrne, C. P. Race, D. R. G. Mitchell, P. B. J. Levecque, N. P. Young, S. M. Holmes, A. Walton, A. I. Kirkland, S. J. Haigh and C. I. Lang, *Nano Lett.*, 2021, **21**, 3989–3996.
42 X. Peng, D. Lu, Y. Qin, M. Li, Y. Guo and S. Guo, *ACS Appl. Mater. Interfaces*, 2020, **12**, 30336–30342.
43 J. L. Reyes-Rodríguez, A. Velázquez-Osorio, D. Bahena-Uribe, A. B. Soto-Guzmán, M. A. Leyva, A. Rodríguez-Castellanos, S. Citalán-Cigarroa and O. Solorza-Feria, *Catal. Sci. Technol.*, 2019, **9**, 2630–2650.
44 N. K. Chaudhari, J. Joo, H. Kwon, B. Kim, H. Y. Kim, S. H. Joo and K. Lee, *Nano Res.*, 2018, **11**, 6111–6140.
45 L. Huang, Z. Jiang, W. Gong and P. K. Shen, *ACS Appl. Nano Mater.*, 2018, **1**, 5019–5026.
46 Y. Zhang, J. Zhang, Z. Chen, Y. Liu, M. Zhang, X. Han, C. Zhong, W. Hu and Y. Deng, *Sci. China Mater.*, 2018, **61**, 697–706.
47 X.-F. Zhang, H.-B. Meng, H.-Y. Chen, J.-J. Feng, K.-M. Fang and A.-J. Wang, *J. Alloys Compd.*, 2019, **786**, 232–239.
48 T. Vicsek, *Fractal Growth Phenomena*, World Scientific, Singapore, 1992, ch. 6.
49 T. A. Witten and L. M. Sander, *Phys. Rev. Lett.*, 1981, **47**, 1400–1403.
50 S. Martineau, *ALEA, Lat. Am. J. Probab. Math. Stat.*, 2017, **14**, 249–270.
51 W. Zhang, in *Nanomaterial. Advances in Experimental Medicine and Biology*, ed. D. Capco and Y. Chen, Springer, Dordrecht, Netherlands, 2014, ch. 2, vol. 811.
52 T. A. Witten and L. M. Sander, *Phys. Rev. B: Condens. Matter Mater. Phys.*, 1983, **27**, 5686–5697.
53 F. Qin, Y. Ma, L. Miao, Z. Wang and L. Gan, *ACS Omega*, 2019, **4**, 8305–8311.
54 F. Gao, Y. Zhang, P. Song, J. Wang, B. Yan, Q. Sun, L. Li, X. Zhu and Y. Du, *Nanoscale*, 2019, **11**, 4831–4836.
55 R. Wu, Y. Li, W. Gong and P. K. Shen, *ACS Sustainable Chem. Eng.*, 2019, **7**, 8419–8428.
56 S. Maksimuk, X. Teng and H. Yang, *J. Mater. Chem. C*, 2007, **111**, 14312–14319.
57 K. J. Jenkinson, Ph.D. dissertation, University of Cambridge, 2019.
58 K. J. Jenkinson, A. Wagner, N. Kornienko, E. Reisner and A. E. H. Wheatley, *Adv. Funct. Mater.*, 2020, **30**, 2002633.
59 K. Chokprasombat, K. Koyvanich, C. Sirisathitkul, P. Harding and S. Rugmai, *Trans. Indian Inst. Met.*, 2016, **69**, 733–740.
60 K. E. Elkins, G. S. Chaubey, V. Nandwana and J. P. Liu, *J. Nano Res.*, 2008, **1**, 23–30.
61 W. Wang, D. Wang, X. Liu, Q. Peng and Y. Li, *Chem. Commun.*, 2012, **49**, 2903–2905.
62 J. Ding, L. Bu, S. Guo, Z. Zhao, E. Zhu, Y. Huang and X. Huang, *Nano Lett.*, 2016, **16**, 2762–2767.
63 S. Mourdikoudis, M. Menelaou, N. Fiuza-Maneiro, G. Zheng, S. Wei, J. Perez-Juste, L. Polavarapu and Z. Sofer, *Nanoscale Horiz.*, 2022, **7**, 941–1015.
64 X. Guo, W. Wang, Y. Yang and Q. Tian, *CrystEngComm*, 2016, **18**, 9033–9041.
65 S. W. Chou, C. L. Zhu, S. Neeleshwar, G. L. Chen, Y. Y. Chen and C. C. Chen, *Chem. Mater.*, 2009, **21**, 4955–4961.
66 S. Sun and H. Zeng, *J. Am. Chem. Soc.*, 2002, **28**, 8204–8205.
67 Y. Yu, W. Yang, X. Sun, W. Zhu, X. Z. Li, D. J. Sellmyer and S. Sun, *Nano Lett.*, 2014, **14**, 2778–2782.
68 S. Sun, C. B. Murray, D. Weller, L. Folks and A. Moser, *Science*, 2000, **287**, 1989–1992.
69 M. Nakaya, M. Kanehara and T. Teranishi, *Langmuir*, 2006, **22**, 3485–3487.
70 X. Teng and H. Yang, *Nano Lett.*, 2005, **5**, 885–891.
71 P. de la Presa, M. Multigner, J. de la Venta, M. A. García and M. L. Ruiz-González, *J. Appl. Phys.*, 2006, **100**, 123915.